Investigation of M-A Constituent in High Strength Steel Welds†

Ivan HRIVNAK*, Fukuhisa MATSUDA and Kenji IKEUCHI*****

Abstract

The metallographic and microfractographical investigations of M-A constituent in the weld HAZ of high strength low alloyed steels are reviewed with particular reference to the internal structure of the M-A constituent, effects of heat treatments on its internal structure and the roll of the M-A constituent in the crack nucleation and propagation on slow bending test and Charpy impact test.

KEY WORDS : (M-A Constituent) (High Strength Steel) (Weld Simulation) (Decomposition) (Ductility) (Impact Properties)

1. Introduction

The weldability of high strength steels is influenced by many factors. The main among them is the steel chemistry and mode of production. Recent metallurgy makes it possible to produce high strength steels with low carbon content, low carbon equivalent values, very fine grains and high purity. Therefore the weldability of high strength steels is very good unless high heat inputs are used in welding. Due to low carbon content and general chemistry of steel, granular upper bainite is formed in heat affected zone (HAZ) or also in weld metal, exhibiting low impact properties. As described by Habraken[1] granular bainite has a composite microstructure of bainitic ferrite together with retained austenite or martensite. But the most important characteristic of granular bainite is the lack of cementite. The transmission electron microscope shows some plates (laths) of bainitic ferrite. The retained austenite is inhomogeneously distributed in the matrix. Sometimes it forms small islands and sometimes it appears as films between the laths, like cementite in upper bainite. The retained austenite may transform during cooling to martensite. The presence of plate martensite islands in the bainitic HAZ of electroslag welds was described long ago[2,3]. Garland and Kirkwood[4] explained the low impact properties of submerged arc welds on Nb-bearing steels as a consequence of martensite-austenite islands present in the bainitic microstructure. This constituent was since then termed as M-A constituent. Although much is now known concerning the transformation behavior, microstructure and its effects on the fracture behavior, our knowledge is still unsatisfactory to explain all the features when welding high strength steels with high heat inputs.

This review gives the summary of the research work made by the division of materials science on the phenomena of M-A constituent in HSLA steels[5,6].

2. Structural Transformations in Welds – The Occurrence of M-A Constituent

Prior to the wide spread use of microalloyed steels, conventional C-Mn steels were welded over a range of heat inputs with only small deterioration in impact properties at higher heat inputs. In weld metals and heat affected zones of microalloyed steels weldments, structure degradation due to strong alloy effect on transformation sequences occurs at compositions which normally would have produced excellent impact properties. Moreover, the chemical composition dependence of notch toughness transition temperature is negligible at the faster cooling rates (lower $t_{8/5}$ values) but important for the higher heat inputs[7]. At slower cooling rates, the microstructure of the HAZ changes from martensite to lower bainite, upper bainite and finally to acicular and proeutectoid ferrite. The usual sequence of nucleation events with decreasing temperature is grain boundary ferrite and a lath structure morphologically similar to side plates which is best termed upper bainite[8]. The side plate structure is observed with

† Received on Oct. 31,1992

* Visiting Professor (Professor, Technical University in Kosice, Kosice, Slovakia)
** Professor
*** Associate Professor

Transactions of JWRI is published by Welding Research Institute, Osaka University, Ibaraki, Osaka 567, Japan

carbide colonies and/or M-A (Martensite-Austenite) islands in between depending on alloy content and heat input. The retained austenite in the M-A island in milder decomposition structures can be partially transformed into pearlite, if very low cooling rates (long cooling times $t_{8/5}$) are used. With higher cooling rates (shorter cooling time $t_{8/5}$) the retained austenite is partially transformed into martensite.

The martensite transformation is accomplished with the maximum expenditure of strain energy by a homogeneous distortion of the austenite. This involves a compression along $[100]_\gamma$ and expansion along $[010]_\gamma$ and $[001]_\gamma$. The strain, forming invariant plane during the $\gamma \rightarrow \alpha'$ transformation can occur either by slip or by twinning. Slip occurs at higher M_S temperatures and twinning at lower M_S temperatures. Martensite has an orientation relationship to the parent austenite, described by Kurdjumov and Sachs, which can be expressed simply

$$(111)_\gamma // (011)_{\alpha'},$$
$$[101]_\gamma // [111]_{\alpha'}.$$

In low or medium carbon steels, the common structure is lath martensite. The structural units - laths - are grouped into packets or sheaves. This martensite has very high dislocation density (10^{15} - 10^{16} m^{-2}). If the martensite has carbon content in excess of 0.20%, its crystallographic structure changes from bcc to tetragonal. With the increasing carbon content the M_S temperature is decreasing. The effect of carbon content on the morphology of martensite and M_S temperature was investigated by Speich and Leslie[9] (see **Fig. 1**). When the M_S temperature is reduced below ~473 K, the microstructure of martensite is changed to plate form. Individual lenticular plates have a substructure of very fine twins spaced about 5 nm apart. The twins can gradually merge into an array of dislocations near the periphery of the plate. The transition from lath to plate martensite is not abrupt[9].

The strength and hardness of martensite are a function of carbon content. In the carbon content range up to ~0.6% the hardness of martensite is a linear function of carbon content, and can be expressed, according to Satoh and Terasaki[10], as

$$H_M = 812 \cdot C + 293,$$

or according to Dueren[11] for pipeline steel welds with carbon content less than 0.2%, as

$$H_M = 802 \cdot C + 305,$$

or according to Yurioka[12] for steels with carbon content up to 0.8% as

$$H_M = 884 \cdot (1 - 0.3 \cdot C^2) + 294.$$

The hardness of martensite as a function of carbon content in Fe-C alloys and steels according to Krauss[13] is given in **Fig. 2**. Due to the increasing amount of residual austenite, the hardness of martensite in steels with carbon

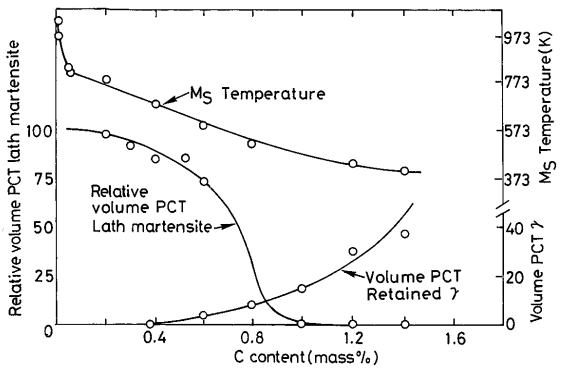

Fig. 1 Effect of carbon content on percentage of lath and plate martensite, M_S temperature and volume % of retained austenite[9].

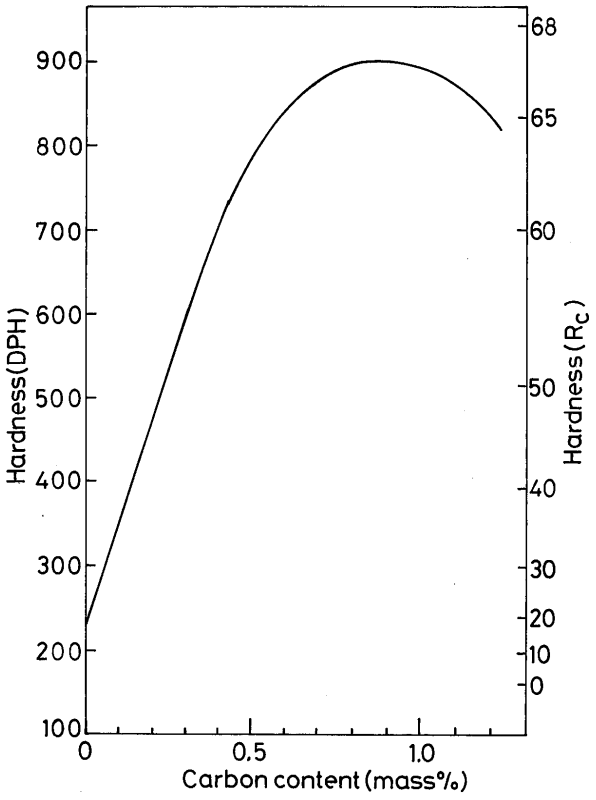

Fig. 2 Hardness of martensite as a function of carbon content[13].

content exceeding 0.8% is decreasing.

As stated above, with the increment of cooling time $t_{8/5}$, the microstructure changes from martensite to lower bainite, upper bainite and finally to acicular ferrite and proeutectoid ferrite. At longer cooling times the transmission electron microscope shows in M-A constituent the presence of cementite particles. Generally the side plate structure has been observed with carbide colonies and/or M-A islands in between depending on alloy content and heat input. The question is whether the

cementite particles present in M-A-C constituent are precipitating from austenite enriched in carbon, or are the result of the self-tempering (autotempering) of martensite in the case that the M_S temperature is well above ambient. The initial cementite morphology in martensite is needle-like when formed during slower cooling or during deliberate tempering. The nucleation sites for cementite are martensite lath boundary or ferrite grain boundaries at higher temperatures. The needles can form array growing in $\langle 100 \rangle_\alpha$ direction and as growth continues, these needles coalesce into massive particles. Pitch and Schrader[14] are giving the following relationships between ferrite and cementite:

$$(211)\,\alpha \,//\, (001)_{Fe_3C},$$
$$[001]\,\alpha \,//\, [100]_{Fe_3C},$$
$$[111]\,\alpha \,//\, [010]_{Fe_3C}.$$

The M-A (M-A-C) constituent forms usually elongated interlath particles in lath upper bainite and blocky particles in acicular ferrite.

The presence of residual austenite is considered to be very harmful for the toughness. Its volume fraction increases with increasing cooling time $t_{8/5}$ as a consequence of carbon enrichment resulting from the increase in diffusion time, and usually is close to 2-6% in the HAZ exhibiting upper bainitic microstructure. According to Verrier et al.[8] the presence of 1% retained austenite will increase the notch toughness transition temperature by 15 K. According to Ikawa et al.[15] retained austenite promotes initiation and propagation of the fracture. Chen et al.[16] observed high stress concentration on the boundary between α-Fe and M-A constituent. At moderate and high temperatures this stress makes the boundary crack or debond. With increasing strain, cracks grow to voids and further develop to deep holes. At lower temperatures, however, stiffer blocky M-A gives rise to concentration and triaxiality of stress at the point near the boundary on the side of ferrite, and makes the later cleavage crack. Very important is the size of M-A. The larger the size, the smaller is the load to make the new crack nucleus initiate.

It is agreed that the M-A constituent has either lath-like or complex (blocky) shape and its volume fraction is usually less than 10% of the total microstructure.

Recently Matsuda et al.[5,6] investigated the M-A constituent in heat affected zones of four boron containing low alloy steels. The thermal cycle of underbead zone (T_{max} = 1623 K) was simulated using the Gleeble instrument. The cooling time $t_{8/5}$ varied from 3.5 to 1000 s. They analyzed the absorbed energy, area fraction of M-A constituent in softer (milder) decomposition products. M-A constituent had either elongated or massive shapes and at cooling times $t_{8/5}$ longer than ~500 s the M-A decomposed into carbides and ferrite. The shape and area fraction of M-A constituent with various simulated condition were the same. The hardness of elongated M-A was 600-800 HV and of massive M-A 800-1200 HV. By the EPMA quantitative analysis 1.3-2.2% C were measured in M-A. Moreover it was recognized that C and Ni were increased in M-A with increasing cooling time.

Higher carbon content in M-A constituent was found by many authors. Recently Josefsson and Andren[17] found 1.14% C in M-A as compared with 0.005% in the surrounding ferrite. Moreover they made a calculation of equilibrium content of carbon in residual austenite. They calculated the temperature-carbon concentration dependence in bainitic reaction, and compared the temperatures at which the austenite and ferrite of the same composition had the same free energy in a stress free transformation with the temperature which additionally took the transformation strain energy into account. Further they supposed the diffusion of carbon but no substitutional alloying elements. They concluded that at 693 K where the bainitic reaction ceases, the expected carbon concentration in austenite is about 2.6 mass%. In their investigation the bainite start temperature (B_S) was determined to be 851 ± 5 K, but the actual transformation started at a lower temperature during continuous cooling between 843 and 693 K.

In the work of Matsuda et al.[5,6], four HSLA steels contained a small quantity of boron (0.0007-0.0012 %). Boron increases hardenability of low carbon steels especially at finer austenite grain size. Austenitizing at higher temperatures reduces the hardenability effect of B. Increasing hardenability does not decrease the M_S temperature. The solubility of B in austenite is very low and the best estimation gives about 0.001% at 1185 K and about 0.005% at the eutectics. To be effective, B must be in solid solution in austenite and not bonded in the form of carbides, nitrides or borocarbides. Boron can easily segregate in austenite grain boundary, and so suppress the nucleation of proeutectoid ferrite by reducing the grain boundary free energy. Evidence is given on the precipitation of $Fe_{23}(C,B)_6$ borocarbides at austenite boundaries.

All steels investigated in Matsuda et al's papers[5,6] contained nickel. Nickel is generally known to increase toughness but this is brought about by lowering the transition temperature rather than by raising the upper-shelf energy.

M-A particles are known to occur not only in weld metals and underbead zones of HAZ but also in intercritical HAZ heated between A_{c1} and A_{c3} temperatures. When welding quenched-and-tempered steels with a microstructure of highly tempered martensite, the transformation $\alpha \rightarrow \gamma$ starts predominantly at former

austenite grain boundary. Small, roundish islands of austenite may transform during cooling to martensite, lower bainite, very fine pearlite or upper bainite in which small portion of M-A is to be found. Similar transformation can occur in the coarse grained underbead zone reheated by the following pass (run) to intercritical range of temperatures. This region is usually called ICGHAZ (Intercritically Reheated Coarse Grained HAZ) and consists of martensite islands (M-A) and tempered martensite. Further welding cycles tend to decompose the M-A constituent. This zone is considered to be LBZ (Local Brittle Zone) although it is still discussed whether the areas containing M-A constituent have to be considered to be LBZ or the main reason for the worst toughness is the occurrence of lath upper bainite structure. The occurrence of M-A manifests itself more markedly in CTOD tests than in notch toughness tests. According to certain criteria[7], every specimen giving a CTOD less than 0.1 mm would include LBZs. Generally, in the CTOD tests there are more severe conditions concerning the constraint, position and sharpness of the crack. The LBZ is also related to "pop-in" phenomenon in CTOD tests. During the stressing of the specimen, the LBZ may crack but the cracks are arrested in surrounding more ductile material.

3. Metallography of M-A Constituent

As stated in the last chapter, the M-A constituent consists of martensite and retained austenite, and may contain cementite precipitated either from austenite (as stated by Habraken and Economopoulos[1]), or as a consequence of lath martensite self-tempering. The study of the fine structure of M-A constituent is difficult because of large extinction in this compound when using transmission electron microscope. Usually pictures like in **Fig. 3** are obtained showing very high contrast in which it is not possible to resolve any details.

We have studied the morphology and composition of M-A in three HSLA steels which have the chemical composition as shown in **Table 1**. These steels were delivered in quenched and tempered conditions. Steel HT 80B was direct quenched.

The occurrence of M-A constituent was observed in simulated underbead zone with peak temperature 1623 K and longer cooling times $t_{8/5}$ over 50 s[5,6]. The main investigation was done in the simulated underbead zone of HT 80B (T_p = 1623 K, $t_{8/5}$ = 200 s).

The effect of the peak temperature and cooling time $t_{8/5}$ on grain size of simulated HAZ is depicted in **Fig. 4**.

Fig. 3 The usual contrast obtained from the M-A particle in transmission electron microscope using thin foil technique.

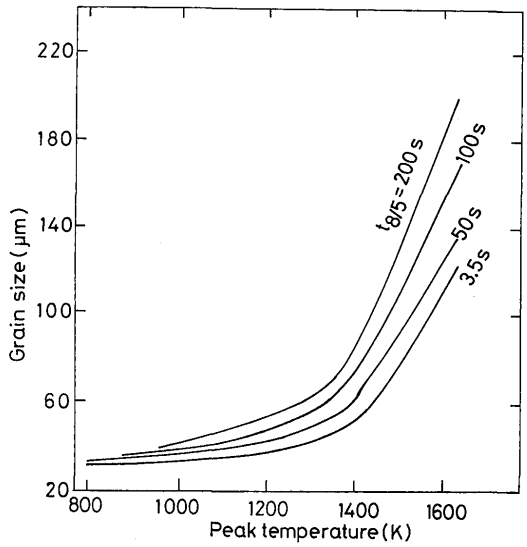

Fig. 4 The effect of peak temperature and cooling time $t_{8/5}$ on the γ-grain size in simulated HAZ of HT 80B steel.

Table 1 Chemical composition of HSLA steels (mass%).

Steel	Thickness (mm)	C	Si	Mn	P	S	Cu	Ni	Cr	Mo	V	Nb	Al	B
HT 80A	60	0.12	0.23	0.93	0.006	0.002	0.19	1.22	0.48	0.45	0.03	-	0.066	0.0007
HT 80B	25	0.10	0.27	0.92	0.009	0.002	0.20	0.98	0.47	0.27	0.04	-	0.052	0.0012
HT 100A	150	0.14	0.05	1.03	0.004	0.001	0.23	3.80	0.56	0.58	0.027	0.012	0.047	0.0011
HT 100B	38	0.11	0.11	0.86	0.004	0.001	0.03	1.57	0.54	0.56	0.073	-	0.053	0.0011

The grains start to coarsen more rapidly at temperatures above 1423 K. Due to very low density and size of second phase particles (AlN, MX), it was not possible to apply the Ashby-Easterling[18] model for the kinetics of grain coarsening.

When using standard etching procedure (2-4% of Nital by immersion) we could identify only M-A islands with cementite precipitated directly from austenite. **Figures 5a** and **5b** characterize the appearance of M-A-C in two cooling times $t_{8/5}$ in HT 80B. As stated in a previous paper[5], the amount of cementite increased with increasing cooling time $t_{8/5}$. Some examples of M-A-C configuration observed with SEM are given in **Fig. 6**.

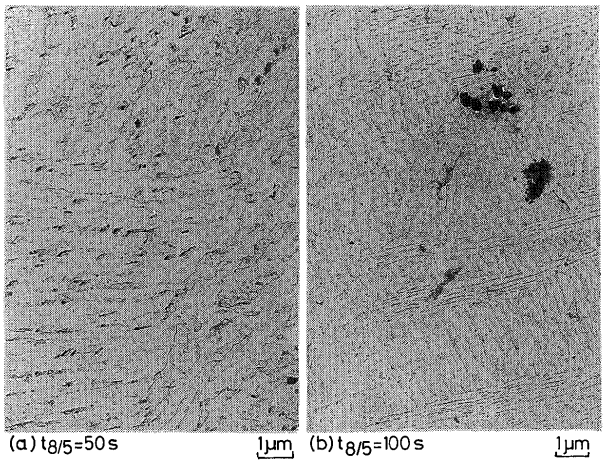

Fig. 5 The appearance of M-A (M-A-C) in simulated HAZ of HT 80B steel at different cooling times (extraction carbon replica). Extracted are cementite particles.

When we used combination of chemical and electrolytic etching we succeeded in extracting great part of the M-A into the carbon replica. **Figures 7a**, **7b** and **7c** show the morphology of extracted particles. Very tiny particles of needle-like or dendrite morphology were identified by selected-area diffraction patterns as cementite Fe_3C. An example of the evaluation of diffraction patterns obtained is given in **Table 2**.

Figures 8a and **8b** characterize the morphology of M-A constituent in dark field image taken from (110) plane of ferrite which nearly coincides with (210) plane of cementite. In many cases the cementite showed tiny dendrite-like morphology which was described by Pitch and Schrader[14] for the early stage of martensite decomposition. From its morphology we can conclude

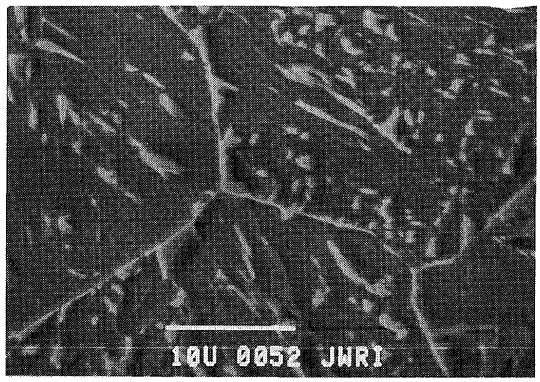

Fig. 6 The distribution of M-A particles (elongated and massive) in the ferritic matrix of simulated HAZ of HT 80B ($t_{8/5}$ = 200 s). Etched in 4% Nital.

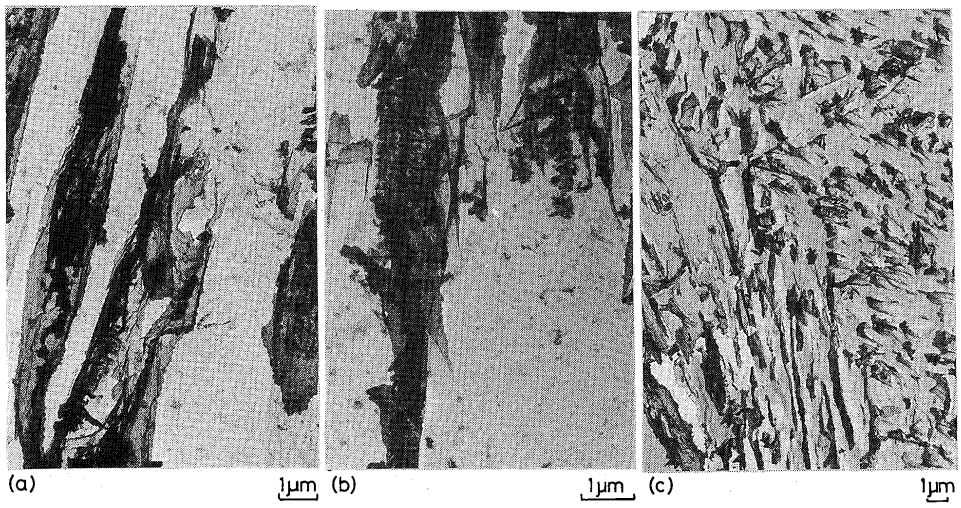

Fig. 7 M-A particles from simulated HAZ of HT 80B steel partially extracted into carbon replica. The tiny and needle-like particles were identified by electron diffraction as cementite Fe_3C.

Table 2 The evaluation of a electron diffraction pattern from Fe_3C.

D (mm)	Intensity	d (nm)	Fe_3C		α - Fe	
			d (nm)	hkl	d (nm)	hkl
13.3	spots	0.254	0.254	020		
14.2	spots	0.238	0.238	112		
-	-	-	0.226	200		
15.6	spots	0.216	0.220	120		
16.1	spots	0.210	0.206	210		
-	-	-	0.202	022		
16.7	spots	0.202			0.2026	110
16.8	spots	0.201	0.201	103		
17.5	spots	0.193	0.197	211		
18.25	spots	0.185	0.187	113		
-	-	-	0.185	122		
19.5	spots	0.173	0.176	212		
20.0	spots	0.168	0.168	004		

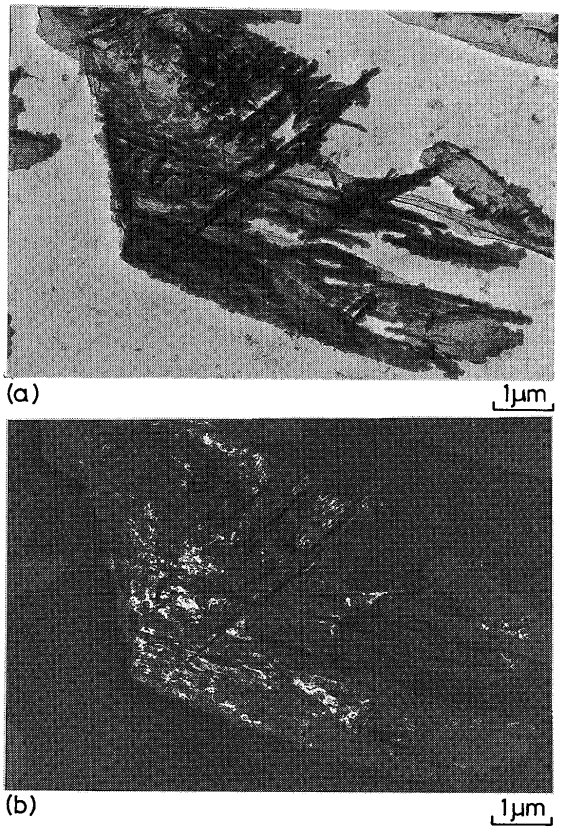

Fig. 8 M-A particles, partially extracted into the carbon replica. Notice the dendrite-like cementite particles precipitated probably during the self-tempering of lath martensite.

that this cementite was precipitated during the self-tempering of martensite in the M-A constituent. When

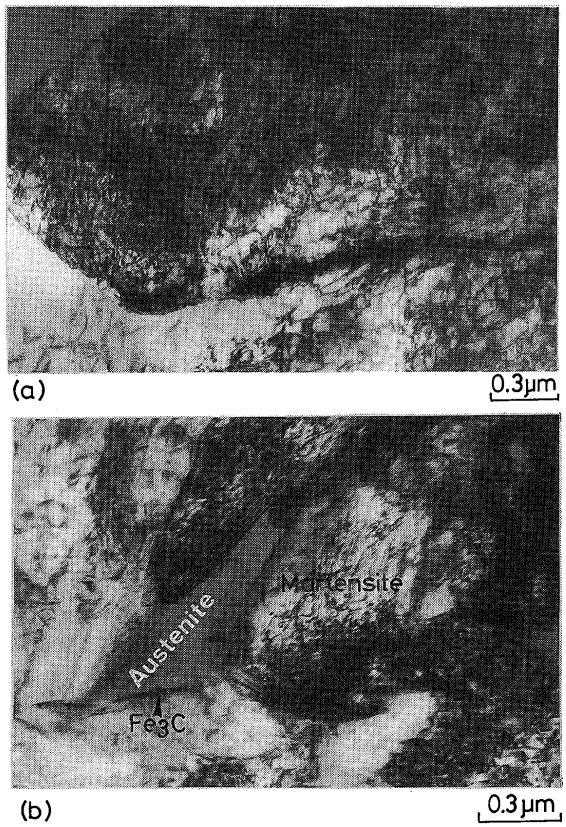

Fig. 9 a) Example of lath martensite in M-A constituent. Notice the very high dislocation density inside the martensite. Martensite is surrounded by ferrite matrix.
b) Example of lath martensite exhibiting high dislocation density, residual austenite and cementite in M-A constituent. Austenite has considerably lower dislocation density than ferrite.

the thickness of thin foils used in TEM was below 200 nm, the fine structure of M-A could be identified. Two types of martensite were detected: lath martensite with very high dislocation density over 10^{15} m^{-2}. The example of such martensite is given in **Fig. 9**. In near vicinity of this martensite, islands of residual austenite were detected by morphology and electron diffraction. **Figure 10** characterizes the occurrence of lath martensite and residual austenite in M-A constituent. In residual autenite some cementite particles are present. **Figure 11** shows an example of α-Fe diffraction patterns in which also diffraction spots of cementite were detected. We could also evaluate the orientation relationships between austenite and martensite. **Figure 12** gives an example of diffraction pattern in which spot patterns of martensite and austenite are present. This diffraction pattern can be explained assuming the Kurdjumov-Sachs orientation relationship.

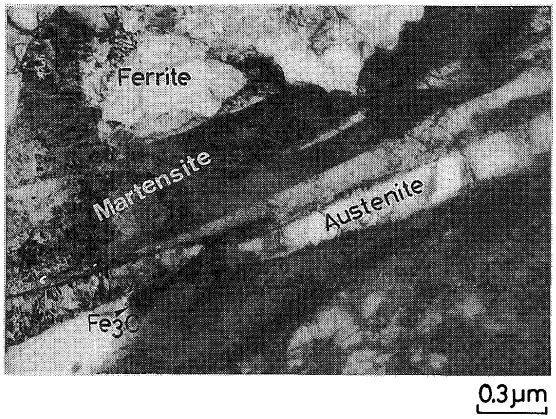

Fig. 10 The complex appearance of M-A constituent. The massive M-A constituent is composed of martensite laths, residual austenite and cementite particles in the boundary between M-A and ferrite matrix. In several parts the laths of martensite exhibite internal twins. The twins are partly entering the laths of residual austenite.

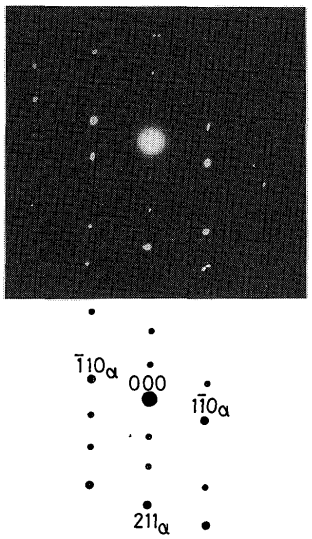

Fig.11 Diffraction spots of ferrite and cementite. The plane of the foil was $(1\bar{1}3)_{\alpha\text{-Fe}}$.

We have also identified the plate martensite exhibiting internal twins. Such examples are given in **Figs. 13-17**. The twins (plates) are oriented in ⟨110⟩ of martensite. **Figures 16** and **17** show the plate-like martensite extracted into carbon replica from steel HT 100A. Residual austenite was in both cases detected in electron diffraction patterns, but could not be found morphologically.

From this investigation we can conclude that in accordance with the published data two kinds of martensite morphology were detected inside the M-A constituent:

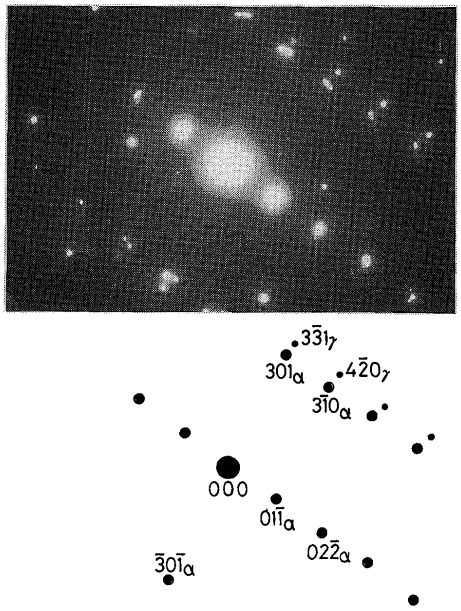

Fig.12 Electron diffraction pattern in which diffraction spots from ferrite and austenite are recorded.

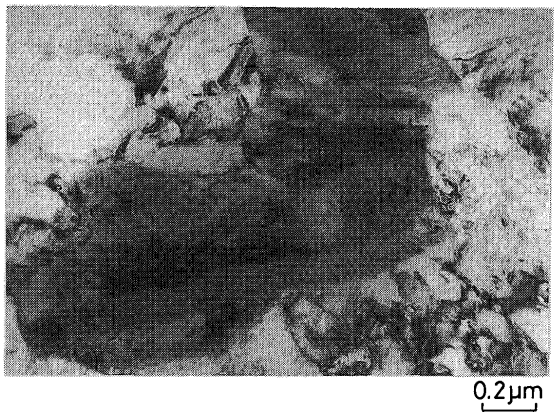

Fig.13 Typical appearance of massive M-A constituent in simulated HT 80B underbead zone. The massive M-A is composed mostly of plate martensite. The plane of the foil is $(111)_{\alpha\text{-Fe}}$.

- dislocation martensite in which laths contain high density of dislocations. This martensite should have higher M_S temperature and during its self-tempering very fine needle-like or dendritic cementite particles are precipitating.
- plate-like martensite in which laths are internally twinned. In this martensite the cementite particles were not found either morphologically or by electron diffraction.

The residual austenite forms islands inside M-A constituent and shows lower dislocation density than surrounding ferrite. Inside this austenite or in the

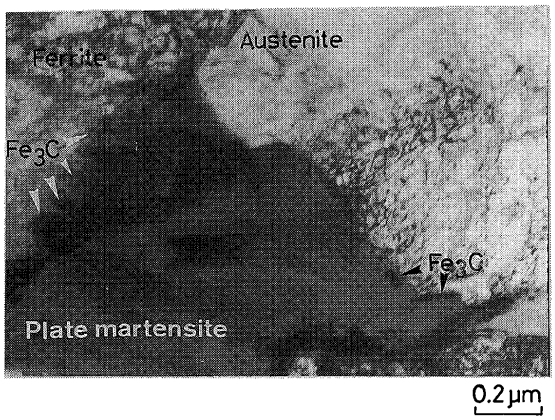

Fig.14 The morphology of massive M-A constituent. Martensite is mostly of plate type. Cementite particles were detected at the interface between martensite and ferrite matrix.

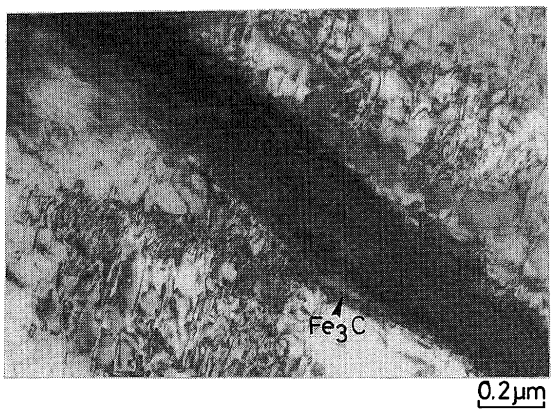

Fig.15 A part of the elongated M-A constituent in the simulated HAZ of HT 80B. The martensite lath contains very high density of dislocations. Notice the smooth transition between M-A and ferrite matrix. The boundary between M-A and matrix is composed of dislocations indicating a high coherency between M-A and matrix.

boundary between austenite and ferrite/martensite, cementite particles of considerably coarse size were found. Two types of cementite were identified in M-A constituents:

- coarser, usually more globular cementite particles inside residual austenite or at the boundary of this austenite. The cementite of this type is precipitated from austenite.
- very fine needle-like or dendritic cementite precipitated inside the lath martensite during its self tempering.

From the above mentioned conclusions we can state

Fig.16 M-A particles extracted into carbon replica from steel HT 100B. In some particles the contours of martensite laths can be resolved but their fine structure is not being resolved.

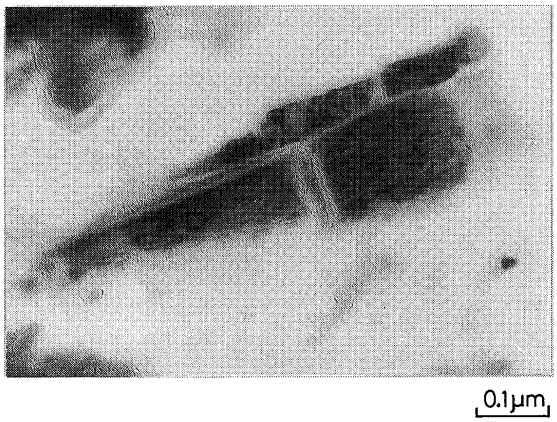

Fig.17 Extracted M-A particle with plate martensite.

that martensite in M-A constituent can have different M_S temperature and the temperature sequences at which the final product of M-A is formed can be characterized as follows:

- temperature at which the structurally-free cementite is precipitated from austenite.
- the M_S temperature of lath martensite.
- the M_S temperature of plate martensite.
- in between tiny cementite can precipitate inside the lath martensite in its self-tempering.

4. The Effect of Peak Temperature and Cooling Time on the M-A Constituent

The effect of peak temperature on the occurrence of M-A constituent was studied in the steel HT 80B, using the cooling time $t_{8/5}$ = 200 s. The corresponding thermal

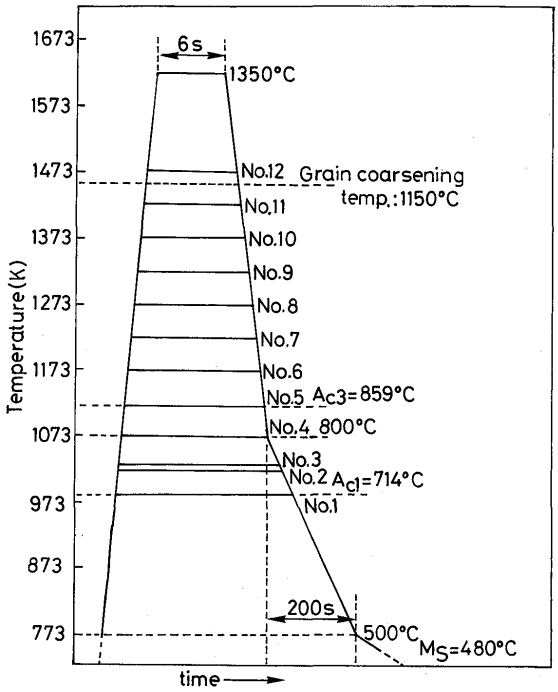

Fig.18 The scheme of the temperature course when simulating the HAZ with different peak temperatures and same cooling time $t_{8/5}$ = 200 s.

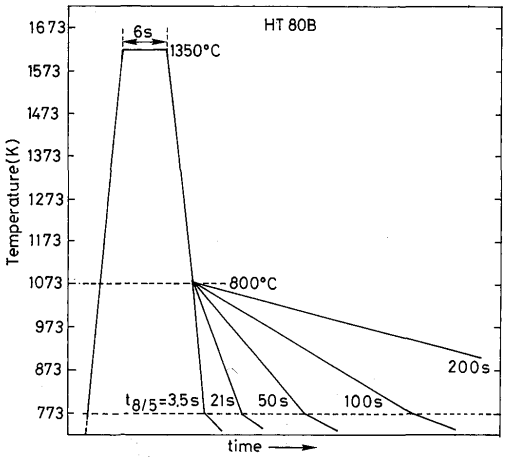

Fig.20 The scheme of the thermal cycles of underbead zone with the peak temperature 1623 K and different cooling rates expressed by the cooling time $t_{8/5}$ = 3.5, 20, 50, 100 and 200 s.

cycles are shown in **Fig. 18**. The transformation from ferrite to austenite nucleates heterogeneously on the boundaries of original γ grains or on inclusions. However, the austenite being transformed does not have a eutectoid but an average carbon concentration in steel. During cooling down at these sites M-A constituent transforms. **Figure 19** gives a sequence of microstructures of specimens with different peak temperatures. In Fig. 19a, the peak temperature was ~1013 K. Transformation $\alpha \rightarrow \gamma$ started at the grain boundary while inside the grain original carbides after tempering the steel are present. The M-A constituent had a massive like morphology. At higher temperatures (Fig. 19b) the portion of $\alpha \rightarrow \gamma \rightarrow \alpha$ transformed area is increased, but still a remarkable part of matrix is not transformed. The presence of coarser carbides from base metal is the proof of this. Only at temperatures above A_{c3} (sample 5) the matrix underwent full transformation $\alpha \rightarrow \gamma \rightarrow \alpha$. In Fig. 19d the left side was not yet fully transformed, while in the right part full austenitization has proceeded. Above this temperature, slow grain growth was recorded (see Fig. 4), which was much more marked at temperatures exceeding ~1423 K. With coarsening of grains the portion of elongated M-A was lesser while the fraction of massive M-A was observed to increase.

The effect of cooling rate expressed in term of cooling time $t_{8/5}$ was investigated in all steels[5], but more thoroughly in steel HT 80B. The scheme of the simulated thermal cycles used is given in **Fig. 20**. Five cooling times 3.5, 20, 50, 100 and 200 s were used in the study. With increasing the cooling time, the microstructure of specimens changed from bainite-martensite mixture ($t_{8/5}$ = 3.5 s, **Fig. 21a, b**) through fully bainitic microstructure ($t_{8/5}$ = 20 s, Fig. 21c, d) to upper bainite or granular bainite in which M-A constituent was determined. In the boundary between M-A and matrix, cementite carbides were often observed. These were extracted into carbon replica and their crystallography was determined by means of electron diffraction. In the last Fig. 21i, j, the M-A particles are partially extracted into carbon replica.

5. Decomposition of M-A Particles in Multipass Welds

In most real cases several weld passes are necessary to complete the joint and the HAZ experiences additional thermal cycles produced by each pass. Although their effect is likely to be small owing to the short duration of the thermal cycle, they can temper or decompose the M-A constituent occurring in the granular bainite.

The decomposition of M-A constituent was studied in the simulated underbead zone of HT 80B with peak temperature Tp = 1623 K and cooling time $t_{8/5}$ = 200 s. The microstructure of this zone, as described above, consisted of granular bainite with the occurrence of ~20% M-A constituent in which partly cementite was found. The decomposition phenomenon was studied by bead-on-plate tests, in which the plate consisted of specimens with simulated underbead zone (see Fig. 29). Further we have

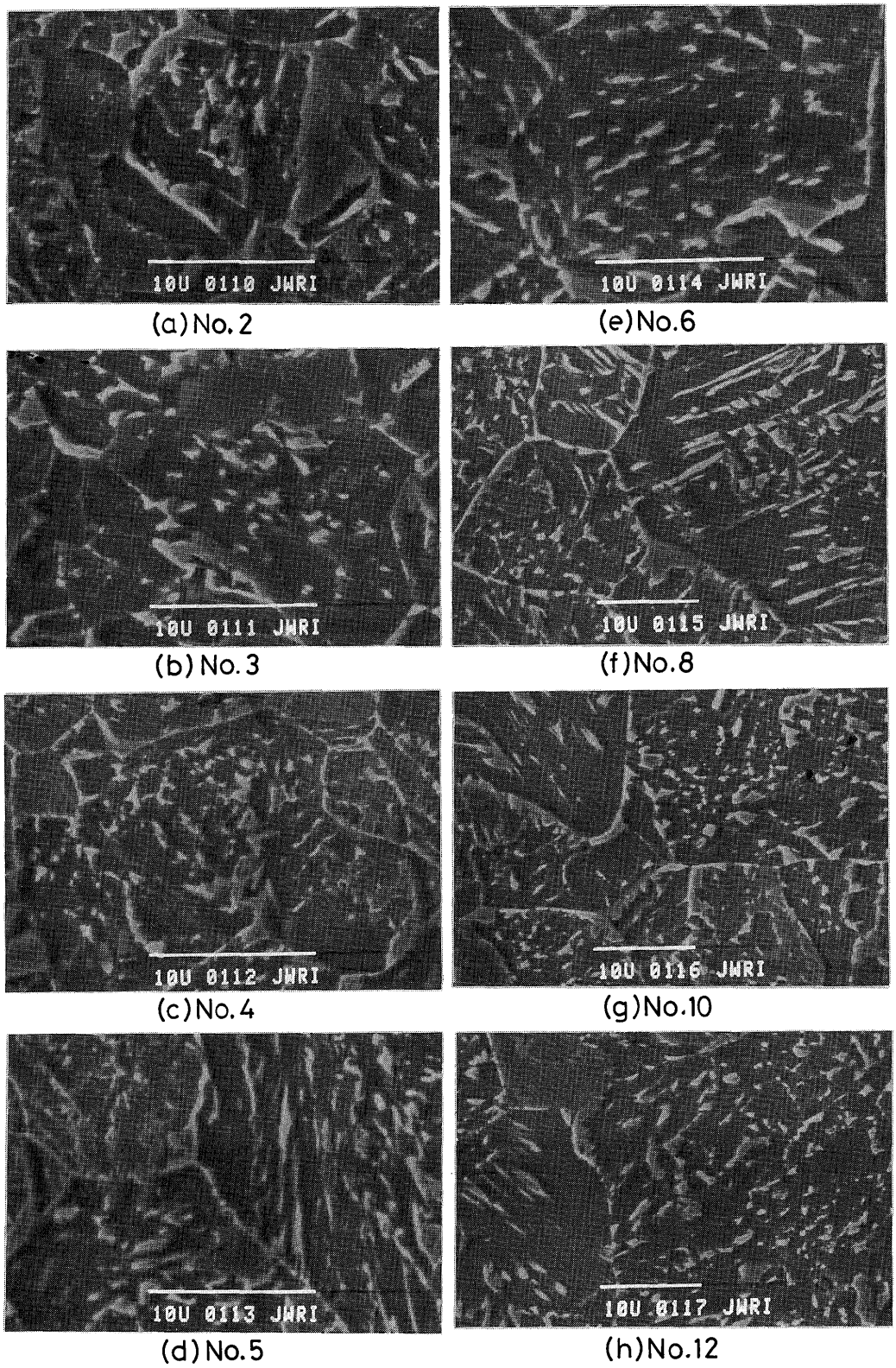

Fig.19 The microstructure of HT 80B subjected to simulated weld thermal cycle of various peak temperatures from Ac_1 up to 1623 K. The structural transformation starts at the former austenite grain boundary a) and proceeds to whole grains when temperature approaches the Ac_3 temperature. Notice the presence of coarse carbide particles in the intercritically heated HAZ. The grain coarsening temperature was determined as 1423 K h).

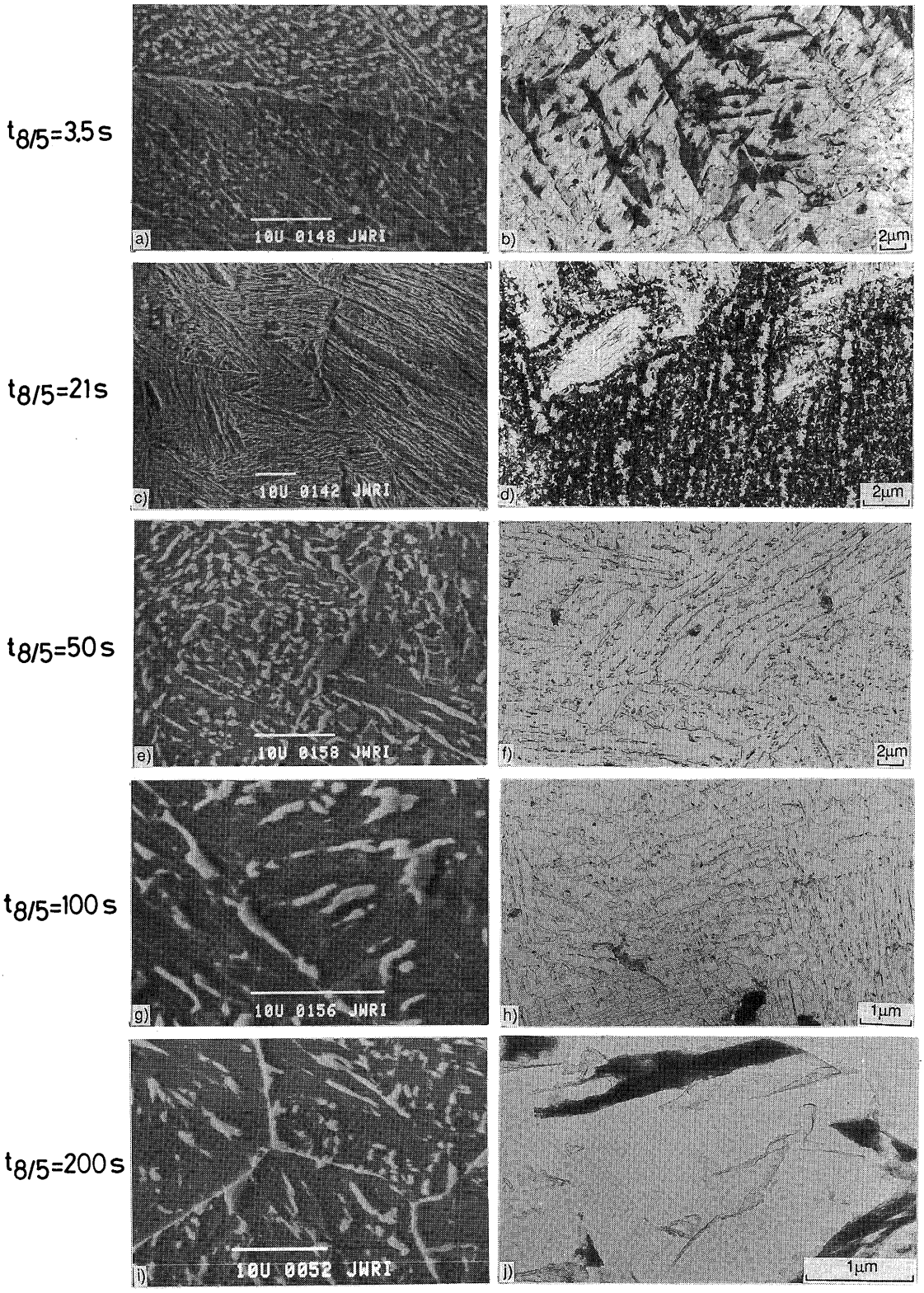

Fig.21 Microstructures of simulated underbead zone with peak temperature 1623 K and different cooling times from 3.5 s a, b) up to 200s i, j). The microstructures on the left side are recorded by means of SEM, and on the right side by means of TEM (extracted carbon replica). In b) extracted are lower bainite carbides, and in d) upper bainite carbides, both of cementite type. The occurrence of M-A (M-A-C) was recorded in e), f), g), h), i) and j). In the last figure the M-A is partly extracted into the replica (the black).

investigated the decomposition of M-A during low temperature tempering at temperatures 523-823 K.

It is known that the several processes occurring during the tempering of martensite involve segregation of carbon to lattice defects, precipitation of carbides, transformation of retained austenite and, finally, recovery and recrystallization of the martensitic structure. These processes are often concurrent. If the M_S temperature is well above the ambient, as it is the case in lath martensite, there is a brief period during which carbon atoms can redistributed themselves to low energy sites associated with dislocation or vacancies. When the M-A is warmed above ~373 K, carbon atoms cluster along {100} prior to precipitation of epsilon Fe_3C carbides. Cementite forms when the tempering temperature is raised above ~423 K. The initial morphology of cementite is needle-like. The common nucleation sites are lath boundaries or ferrite grain boundaries at higher temperatures. Retained austenite decomposes to bainite at tempering temperatures of 473 to 573 K or directly to cementite and ferrite.

The recovery of defect structure of martensite begins at temperatures above 673 K, when martensite laths are annihilated and a fine polygonal grain structure is developed. The final structure of highly tempered granular bainite, containing M-A particles consists of ferrite grains with carbides scattered throughout. Due to high carbon content in M-A constituent, the precipitation of ε-carbides or cementite occurs very quickly. After the precipitation of rod-shaped Fe_3C particles a recovery of defect structure inside the M-A constituent is proceeding, sferoidisation of carbide particles, recrystallization and their growth. When the steel contains carbide-forming elements like Cr, Mo and V, a secondary hardening may occur in the temperature range from 773 to 873 K, because of the re-solution of Fe_3C and precipitation of alloy carbides like Mo_2C. Molybdenum carbides form needles about 10 nm long and 2 nm in diameter.

Figures 22a-22d show various stages of the M-A decomposition during tempering of HAZ above 523 K. In massive M-A particles, needle-like cementite precipitates predominantly at M-A/matrix boundaries (Fig. 22c). In elongated M-A (Figs. 22a and 22b) the precipitation of cementite was observed throughout the grains. At temperatures above 573 K recovery of M-A matrix is observed, and at temperatures above 673 K the resulting microstructure can be described as ferritic carbide.

As mentioned above the tempering effect of additional thermal cycle caused by next welding passes is likely to be small. But if the heat input used is high enough (as it is in our case, characterized by $t_{8/5}$ = 200 s), then the tempering effect of subsequent passes cannot be neglected. Then in the zone, heated to temperatures

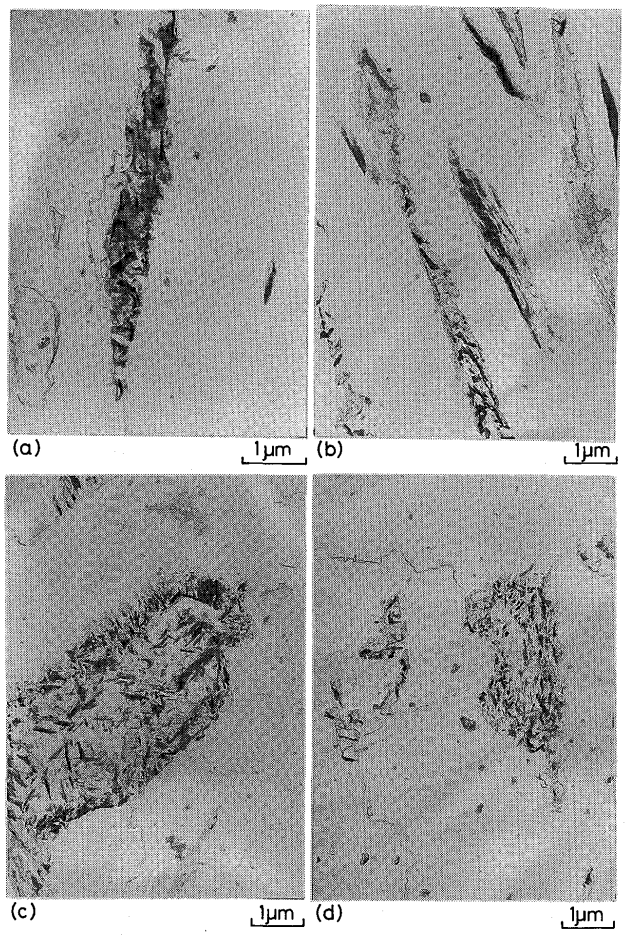

Fig.22 Characteristic stages of the M-A decomposition in HT 80B. In the elongated M-A the precipitation of needle or rod-like cementite particles was observed throughout the size of M-A as shown in a) and b). In massive M-A constituent the precipitation of cementite was more marked at the boundaries between M-A and matrix (see c)). Notice the Widmanstätten precipitation of cementite rods inside the M-A particle. Figure d) characterizes an intermediate stage of M-A decomposition in which cementite is starting to coarsen or re-dissolve.

above 673 K complete decomposition of M-A takes place. As seen in **Fig. 23**, coarse, mostly globular carbides were precipitated predominantly at grain boundaries and boundaries of M-A with the matrix. Inside the former M-A constituent finer precipitates were found in some cases like **Figs. 24** and **25**. According to their morphology and size, they could be molybdenum carbides or MC.

It can be concluded that the M-A constituent decomposes similarly during tempering or welding. In the temperature range of 523-673 K the main decomposition product is needle like cementite carbides and at higher

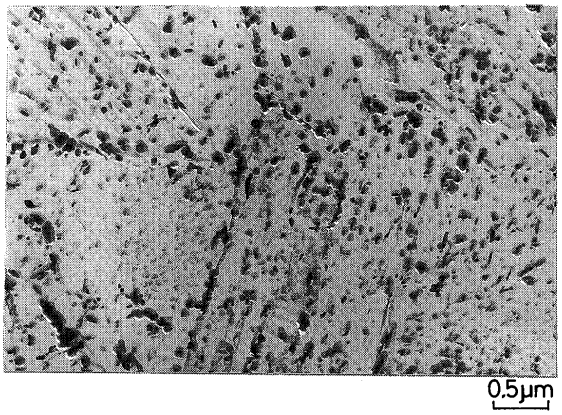

Fig.23 Decomposition of M-A into ferrite-carbide structure. Notice the higher concentration of cementite at former austenite grain boundary and interlath areas. Coarse carbides were identified by electron diffraction as cementite. Very fine precipitates inside the former massive M-A were identified as Mo_2C.

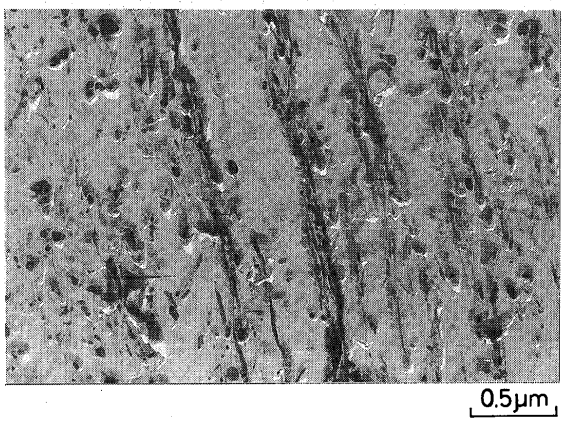

Fig.24 Example of preferred precipitation of cementite carbides at the laths boundaries.

temperatures re-solution of these carbides and precipitation of coarser, mostly globular cementite, alloyed by other carbide forming elements present in the steel. Inside the former M-A particles precipitation of fine Mo_2C carbides was found. The residual austenite has decomposed to ferrite and carbides.

6. Intercritical HAZ in HT 80B

In the partially transformed intercritical region, a wide variety of microstructures can be formed, depending on chemical composition, previous heat treatment and rate of cooling. In the heating-up region, at temperatures between A_{c1} and A_{c3}, only carbon rich constituents form austenite, the remainder is unchanged. Which type of

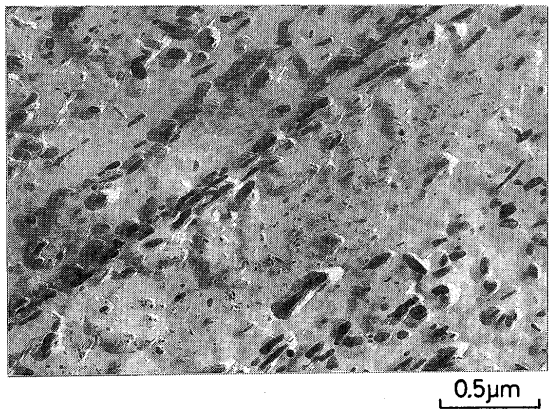

Fig.25 Example of high temperature (above 673 K) decomposition of M-A to carbides and ferrite. The coarser carbides at the boundary of former M-A constituent are of cementite type, the very fine carbides inside the former M-A are either Mo_2C or MC.

constituent would form from the carbon rich austenite is determined by the subsequent cooling rate. If, however, the microstructure of parent material is composed of highly tempered martensite, as it is in our case, the austenite nucleates and grows preferentially along the prior austenite grain boundaries, between bainite laths and between martensite laths.

We have investigated the effect of cooling rate (expressed in the term of cooling time $t_{8/5}$) on the microstructure of intercritically affected HT 80B steel. The scheme of simulated thermal cycles used in these tests is given in **Fig. 26**. Five cooling rates, corresponding to cooling times $t_{8/5}$ = 3.5, 20, 50, 100 and 200 s were used with peak temperatures 993-1003 K.

For better orientation, **Fig. 27** characterizes the whole intercritically affected region where the microstructural changes starting with the occurrence of small islands of transformed phase up to fully transformed matrix are seen.

As expected, at the faster cooling time (3.5 s) the microstructure of the transformed islands is composed of martensite and bainite (see **Figs. 28a** and **28b**). At cooling time 20 s the microstructure of transformed islands turns to bainite (Figs. 28c and 28d) with small portion of martensite and at cooling time 50 s it is nearly upper bainite with great portion of martensite (Figs. 28e and 28f). The presence of M-A constituent in the transformed islands was clearly detected in cooling time $t_{8/5}$ = 100 s (Figs. 28g and 28h), while in the longer cooling time (200 s) the microstructure of transformed islands could be characterized as granular bainite with cementite particles and M-A constituent.

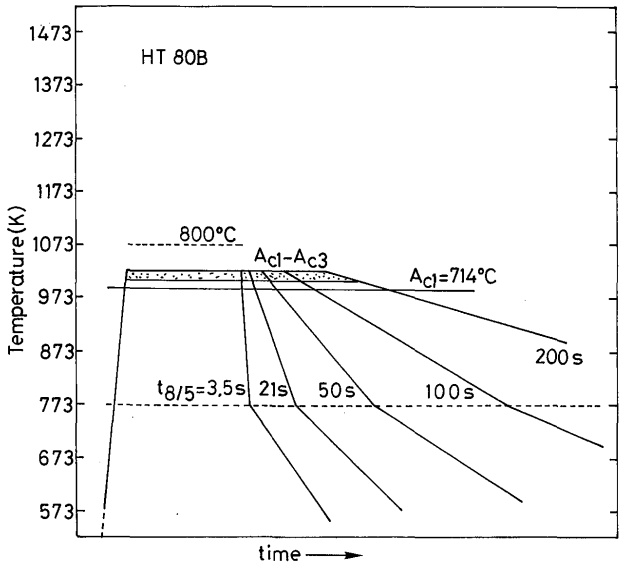

Fig.26 The scheme of the temperature course when simulating the intercritical thermal cycles using peak temperature in the range 1003-1013 K and different cooling rates which correspond to cooling times $t_{8/5}$ = 3.5, 20, 50, 100 and 200 s.

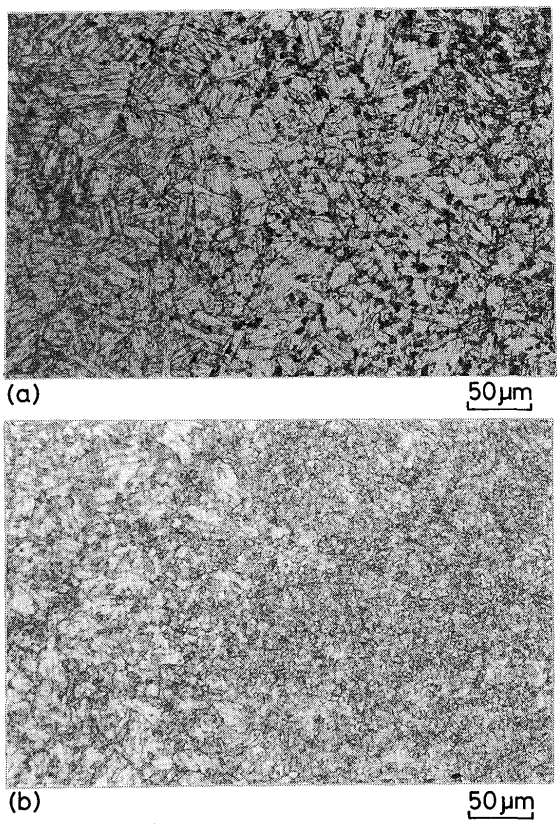

Fig.27 The microstructure of intercritically affected HAZ in HT 80B corresponding to cooling time $t_{8/5}$ = 200 s.

We can conclude that in the intercritically affected region the transformation from ferrite to austenite starts at the former austenite grain boundaries. Islands of austenite can - in dependence on the cooling rate - transform to martensite, heterogeneous mixture of bainite and martensite, bainite or granular bainite with cementite carbides and M-A constituent in it. As mentioned above, this zone is included among the LBZs.

7. Intercritically Reheated Grain Coarsened HAZ (ICGCHAZ)

In the previous chapter we have discussed the microstructural changes occurring in the intercritically heated zone and concluded that this zone can be considered as LBZ, when welding high strength microalloyed steels. This zone exhibits low fracture toughness. Although initially only coarse grained and intercritically affected HAZ was considered as LBZ, number of studies have indicated that the location of LBZ can vary. The region, referred to as the intercritically reheated coarsened HAZ (ICGCHAZ), containing large microphases, consisting of M-A constituent, can also be considered to be LBZ and contribute to embrittlement.

We have studied the microstructural changes and corresponding hardness changes in the coarse grained HAZ which exhibited large amount of M-A constituent and was reheated intercritically by the subsequent welding pass . In HT 80B steel the effect of high heat input welding has been simulated by applying thermal cycles in which T_p = 1623 K and cooling time $t_{8/5}$ = 200 s. The microstructure of this zone was described in chapter 3. We used these simulated specimens as parent material for the bead-on-plate tests with 1, 2 or 3 weld beads. The beads were deposited by MIG process in which 306 kJm^{-1} heat input was used. The chemical composition of the welding wire corresponded to HT 80B steel. We have studied the microstructural changes:

- in the heat affected zone under the weld bead, where the 'parent material' was the previously simulated underbead zone, and
- in the intercritically affected original HAZ that means the intercritically affected intercritical HAZ of HT 80B.

For illustration, **Fig. 29** characterizes the welding situation, and **Figs. 30** and **31** show the results of hardness measurements (HV) across the weld (Fig. 30) and across the intercritically reheated intercritical zone (Fig. 31). From Fig. 30, it can be seen that in the new HAZ hardness is decreasing. The remarkable softening has occurred in the intercritically reheated HAZ which makes 35 HV for 1 bead, 50 HV for 2 beads and 60 HV for 3

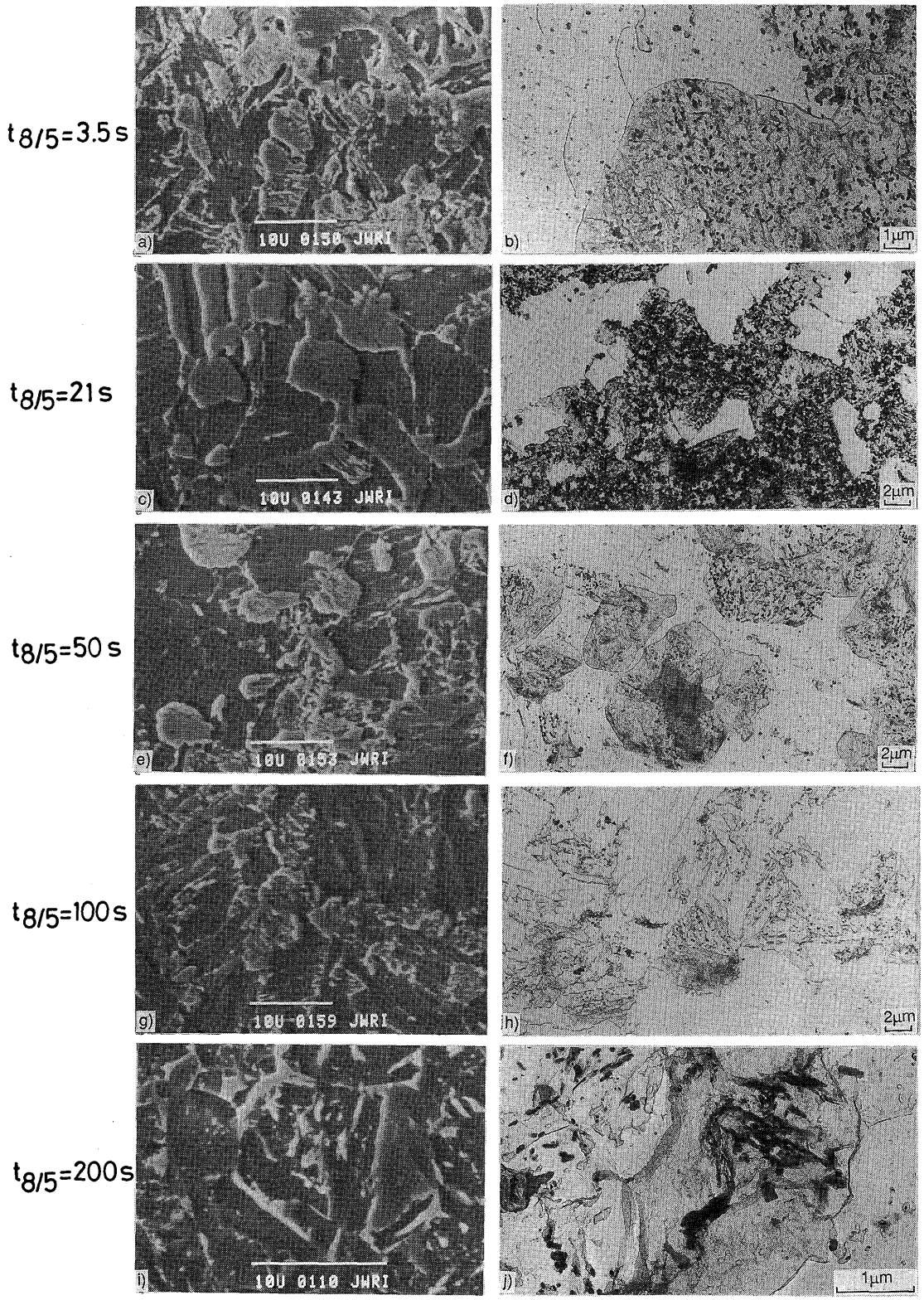

Fig.28 The microstructures of intercritically affected HAZ with various cooling rates corresponding to cooling times $t_{8/5}$ = 3.5 s a, b), 20 s c, d), 50 s e, f), 100 s g, h) and 200 s i, j). The microstructures on the left side were recorded with SEM, and those on the right side with TEM.

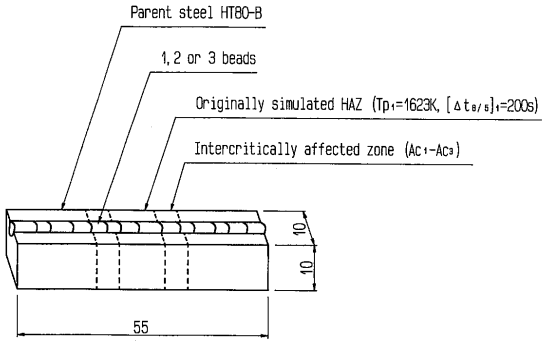

Fig.29 The scheme of bead-on-plate test in which simulated specimens of HT 80B were used as base metal, and one, two and three beads were deposited using the heat input of 306 kJm^{-1}.

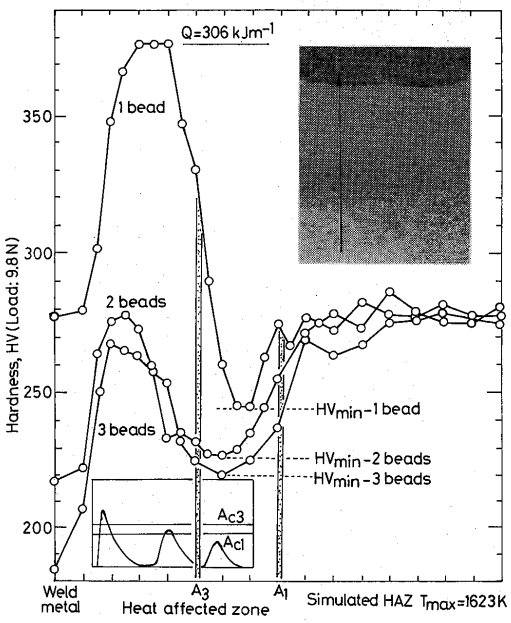

Fig.30 The hardness course through the heat affected zone in bead-on-plate test in which 1, 2 or 3 layers were deposited.

beads. The corresponding microstructural situation is characterized in **Fig. 32**. **Figure 33** gives an example that the structural transformation can start also in previous M-A constituent and this can be considered as indirect proof of higher carbon content in it. The original M-A constituent starts to decompose at temperatures above 523-573 K. **Figure 34** shows an example of M-A decomposition connected with fine cementite carbide precipitation.

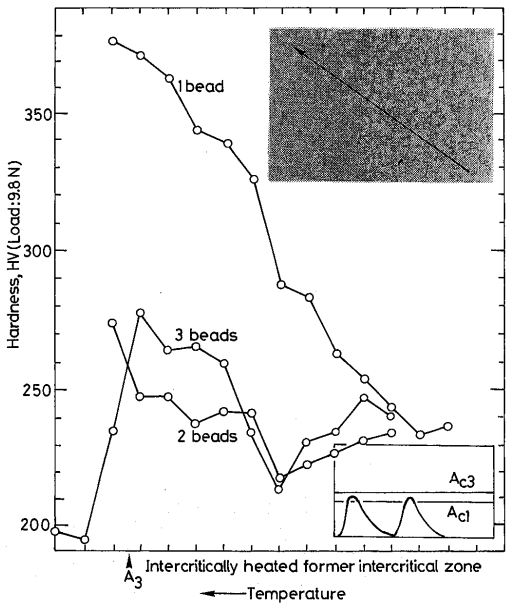

Fig.31 The hardness course through the intercritically reheated intercritical HAZ of HT 80B.

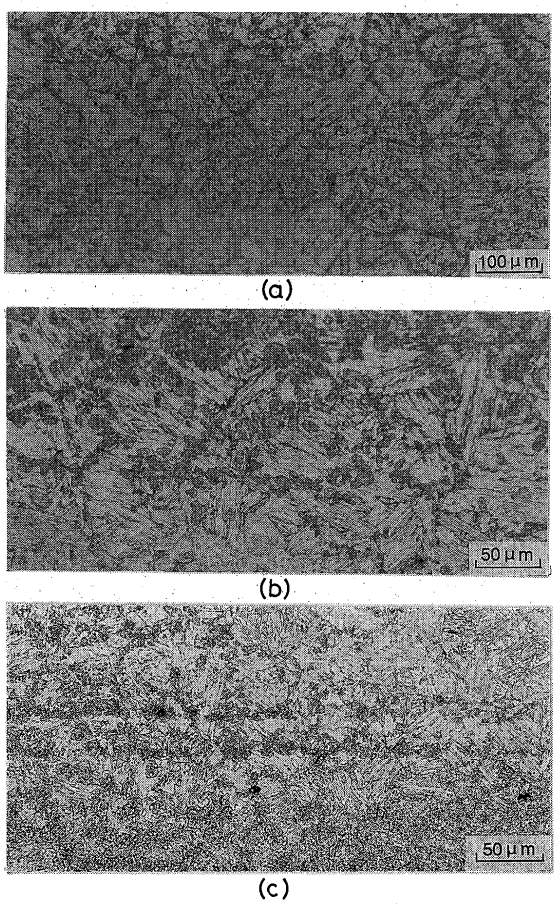

Fig.32 The microstructure of intercritically heated HAZ of underbead zone of HT 80B when using 1 a), 2 b) or 3 c) weld passes.

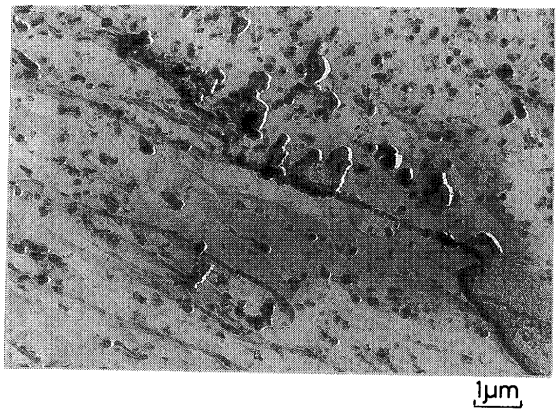

Fig.33 The transformation $\alpha \rightarrow \gamma$ starts also at the former M-A constituent.

8. Effect of M-A Constituent on Ductility and Impact Properties

Slow-rate bending tests were used with maximum straining rate 0.3 mms^{-1} and maximum straining log ε = 0.7 on the tensile side of the specimen. Deformation was carried out at 5 different temperatures (ambient, 273 K, 253 K, 213 K and 77 K). The behavior of M-A during straining was evaluated on metallographic polished and etched specimens taken from the strained area. At room temperature as well as at temperatures down to 213 K the deformation ability of the simulated underbead zone (T_p = 1623 K, $t_{8/5}$ = 200 s) was good. At the temperatures of solid carbon dioxide (213 K) and liquid nitrogen (77 K), however, the specimens fractured nearly at nil deformation.

At temperatures above the ductile-brittle transition the fracture mechanism changes from brittle or cleavage fracture to ductile fracture by microvoid initiation, growth and coalescence. Microvoids are initiated at interfaces between the matrix and particles such as carbides, precipitates and inclusions, and also at imperfections such as microporosity and microcracks, grain boundaries, cleavage planes or at any site where a discontinuity concentrates the plastic flow. The total absence of second-phase particles would result in fracture by 100% reduction of area. It is also possible for fracture to occur by microvoids coalescence within a slip bands. All these phenomena can affect the ductility of steel.

There are two main factors which could influence the ductility of simulated underbead zone of HT 80B. At first this is the occurrence of second phase particles - in our case inclusions and the M-A constituent. Separation at the site of microvoid initiation can occur across a second-phase particle or at a particle-matrix interface. At second

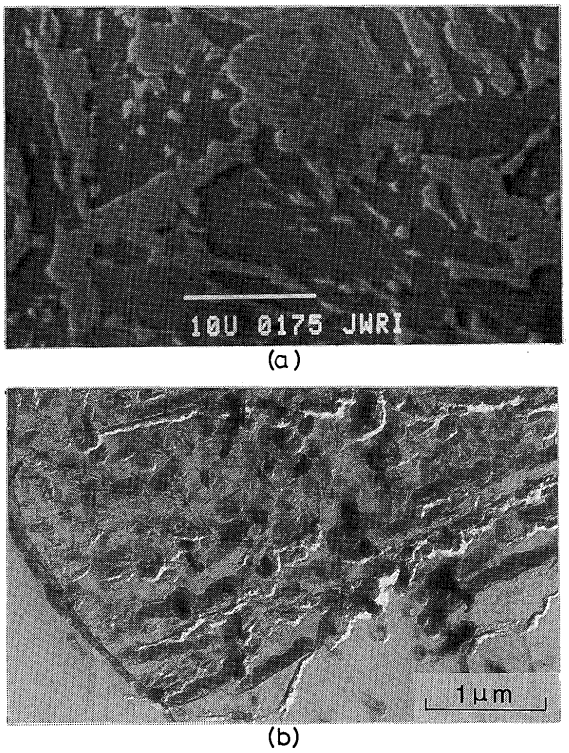

Fig.34 The decomposition of former M-A constituent by the heat of subsequent pass. a) general appearance with SEM, and b) detail with TEM.

there are coarse grains which may also concentrate the stress at the end of slip bands and grain boundaries. And as the larger the grains, the longer will be the slip bands and greater stress concentration.

As mentioned above we have observed the effect of M-A particles in the deformation and fracturing process on the surface of metallographic specimens. Usually the polished surface was etched prior to deformation. When crack or fracture appeared, we could simultaneously observe the etched surface of the specimen and the corresponding fracture, because of the deep distance of focus of scanning electron microscope. It is known that stress triaxiality is higher inside the specimen than in its surface. Therefore we have prepared metallographic specimens also in the bulk of the specimen in planes perpendicular to fracture surface. And, finally, to resolve better the configuration of M-A particles on fracture surfaces, fracture surfaces were etched in Nital, too. Evaluating the results of great many tests, we can conclude that in the ductile temperature range the M-A particles exhibited a good straining ability. Only at high strains the particles cracked or were fragmented. Several cases are shown in **Figs. 35a-35d**.

In Fig. 35a an example of elongated M-A constituent fragmentation is shown. It must be pointed out, however,

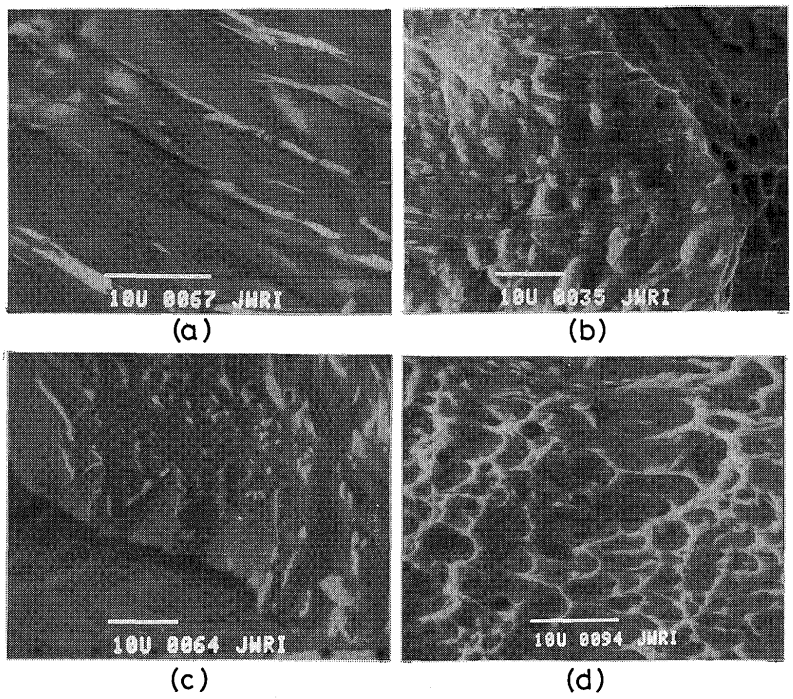

Fig.35 Examples of behavior of M-A during slow rate straining.

that M-A constituent contains some portion of cementite which is brittle in nature and during the straining of M-A it may fracture first and act as stress/strain concentrator. Figure 35b was taken from the transition to the dimple fracture surface, and a progression of some M-A particles fragmentation and dimple initiation were shown in it. The dimple size appears to depend on the number of microvoid-initiation sites available and the relative plasticity of the matrix. Another example of the dimple structure is given in Fig. 35d. Large M-A particles that fracture by cleavage have little effect on matrix dimple size, but smaller particles that act as microvoid-initiation sites influence dimple shape more strongly. When etching the dimpled fracture surface, we could not reveal more M-A particles, as seen inside the dimples.

When the stress triaxiality is higher or the straining temperature is lowered, we could better resolve the microvoids initiation and coalescence at the M-A/matrix boundary. **Figures 36a-36f** are giving some examples. Figures 36a characterizes the initiation of microvoids on either side of M-A constituent, and a crack by coalescence of microvoids in the upper part of the figure. In Fig. 36b microcrack is present on both sides of M-A constituent. Figure 36c shows that the crack initiation site may be at the grain boundary, too. If crack has already initiated, it can propagate in such a manner that the M-A particles intersects. Such example is given in Fig. 36c. But we have also observed cases in which the M-A particles acted as an obstacles against propagating cracks and the crack was kinked out from its original path (Fig. 36d), or when the crack reached the M-A particle, it was arrested, but the particle itself was cracked, too (Fig. 36d). These phenomena were more clearly visible when the straining temperature was lowered near to ductile-brittle transition temperature and the main mode of fracture was cleavage with the occurrence of many secondary microcracks. One example is given in Fig. 36e in which the main cleavage fracture is intersecting the M-A particle, or in Fig. 36f which characterizes the stretch zone at the tip of the crack. From the investigation, we can conclude that the M-A constituent would adversely affect the ductility of the steel. Microvoids can nucleate on either side of the M-A constituent, but in ferrite matrix. The M-A acts a role of stress concentrator. At higher steps of straining M-A cannot withstand the deformation bearing by the matrix and cracks, or is fragmented. Fragmentation is occurring firstly in the cementite part of M-A. M-A can crack also as a consequence of its intersection with propagating secondary crack. In explaining the effect of M-A constituent on the ductility of weld, we may not forget the similar and may be more pronounced effect of coarse grains in this area. Coarse grains makes possible the longer slip band and consequently greater stress concentration.

The effect of M-A constituent on impact properties of simulated underbead zone of HT 80B was studied by

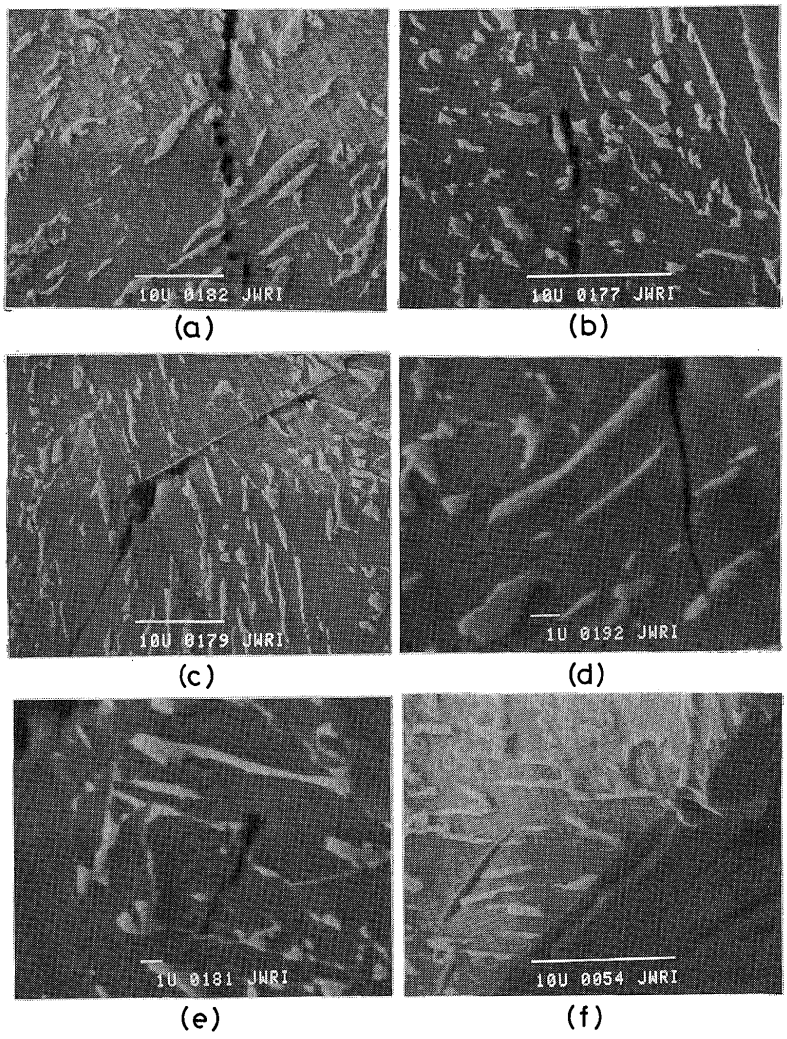

Fig.36 Examples of voids nucleation, growth and occurrence of cracks at both sides of M-A particles, and intersection of secondary cracks with M-A particles.

dynamic bending test of notched rods (10 × 10 mm) at various temperatures from the ambient down to 77 K. It was reported[5] that the notch toughness values (KV) of simulated specimens are very low at room temperature (below 40 J to be compared with 260 J of the parent material). Marked drop of notch toughness was recorded at cooling times over 50 s when upper bainitic structure with the presence of M-A constituent appeared.

The main mode of fracture on these tests was cleavage. It is generally agreed that the major cause of brittle fracture is inability of the matrix to resist crack propagation through relaxation of stress at the crack tip by local plastic flow. If time is not sufficient to allow for stress relaxation, the crack will spread rapidly. Several metallurgical phenomena affect the ductile-to-brittle fracture transition in structural steel. We have already mentioned the embrittling effect of large grains. Second phase particles, like M-A, are detrimental to fracture toughness, especially if located at grain boundaries.

The observed mode of impact fracture in the ductile temperature range was the same as in the slow-rate straining tests and the resulting fracture was composed of dimples mostly. It is supposed that the M-A particles decrease the upper shelf energy in similar manner as they influence the ductility.

In the temperature range below the ductile-brittle transition the mode of fracture on impact tests was predominantly cleavage in which the fracture path followed a transgranular plane, which was one of the $\{100\}_{\alpha\text{-Fe}}$ planes. The fracture planes changed orientation from grain to grain, which resulted in branching of the crack. The river patterns, representing

steps between different local cleavage facets of the same general cleavage plane, were well defined. The presence of M-A particles was recorded at the edge of river patterns. Higher amount of secondary cleavage cracks were observed also in metallographic specimens prepared from the inside of the fractured rods. Some examples are given in **Figs. 37a-37e**. It is seen that in some cases secondary cleavage cracks intersects the M-A particles, but in many cases secondary cleavage crack was arrested or kinked out by the M-A particle. In Fig. 37a, some M-A particles are intersected, but some remained unaffected. This is better seen in Fig. 37b in which the particles were intersected but the other caused a step in the cleavage fracture. The situation is, in general, characterized by Fig. 37c in which also the corresponding fracture surface (on the right side) is etched. The effect of M-A particles on the occurrence of river patterns is seen also in Fig. 37e in which the microstructure (left side) and the corresponding fracture surface (right side) are recorded. In other cases the matrix itself was tough enough to arrest the propagating secondary crack and at the tip of the crack a stretched zone was observed (Fig. 37d). The M-A particles were recorded to act as local dimple fracture initiation.

Figures 38a-38c give other examples in this study. We have seen already in Fig. 37c that the cleavage crack surface has similarly high density of M-A particles as the polished surface. In Fig. 38a higher concentration of M-A particles at the river edges supports the explanation that M-A can change the cleavage fracture plane. Moreover this figure supports the view that M-A particles have some crystallographic orientation relationship with the matrix. The fracture planes in Fig. 38a are $\{100\}_{\alpha\text{-Fe}}$ planes and the orientation of M-A particles is also $\langle 100 \rangle_{\alpha\text{-Fe}}$. But in Fig. 38b, in which the fracture surfaces are also formed by cubic planes, the orientation

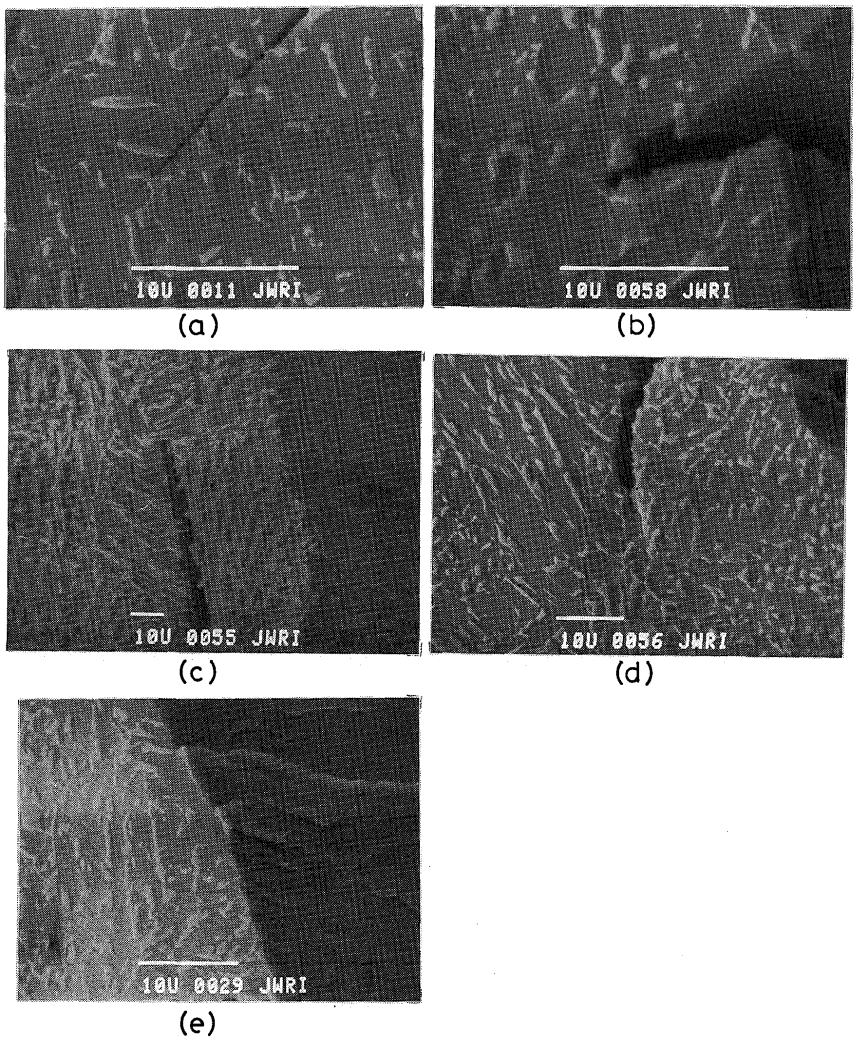

Fig.37 Interactions of M-A particles with secondary cracks and the effect of M-A particles on the fracture path.

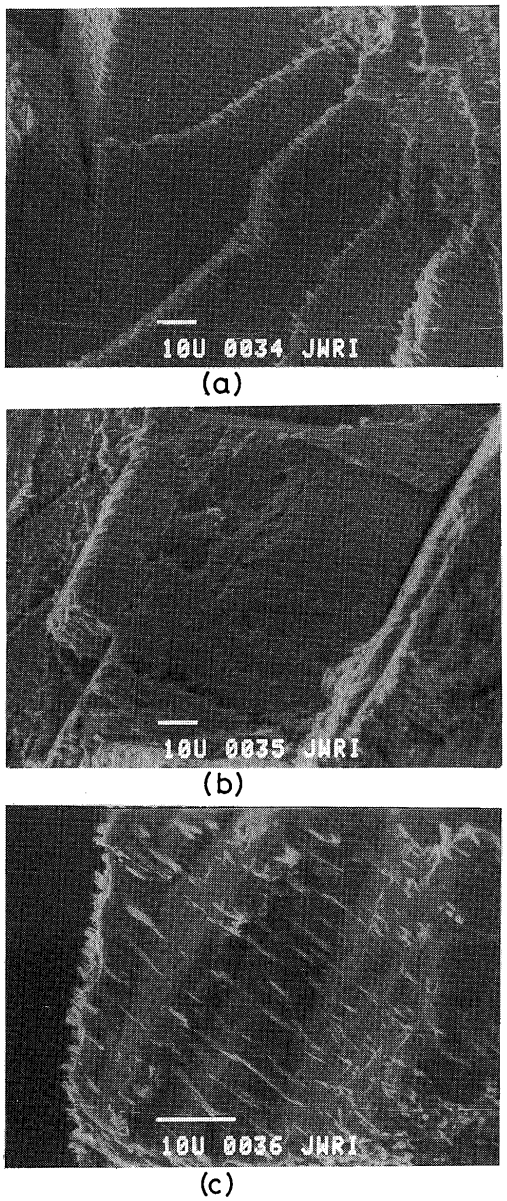

Fig.38 The morphology of M-A constituent of the etched fracture surfaces.

of M-A particles is declined by ~30° from $\langle 100 \rangle_{\alpha\text{-Fe}}$. Intersecting is also seen in Fig. 38c in which the fracture surfaces were dissolved during etching and M-A particles remained at the fracture plane.

This study has revealed that M-A particles contribute to brittleness of the weld by reinitiating the cleavage fracture. The reinitiating cracks were found to occur on either side of M-A constituent due to high stress concentration in surrounding ferrite matrix. As reinitiating sites also cracked M-A particles were found. On the other hand it must be pointed out that the same reason for brittleness are the coarse grains in the underbead zone. Therefore it is difficult to evaluate the contribution of M-A particles and the effect of grain coarsening to the zone embrittlement. We have also shown that in some cases the M-A particles can act as obstacles in propagating cleavage fracture and contribute to increase the fracture energy.

9. General Discussion

In the previous chapter, we have described the experiments and results obtained concerning the M-A constituent in HAZ of HT steels. It was shown that M-A constituent is a compound of upper bainite or granular bainite and results from the retained austenite after the transformation of ferritic laths. As the last compound to be transformed, this austenite is enriched in carbon. Based on thermodynamic consideration the expected carbon concentration in austenite is about 2.6 mass%. Higher carbon content in M-A constituent was found by many authors. We must but not forget that at higher temperatures cementite can precipitate from this austenite. Precipitation of cementite from austenite was described e.g. by Habraken[1] or by the author[19,20]. When measuring the carbon content in M-A constituent it is not clear whether this is an average carbon content, carbon content found in cementite or in pure martensite or retained austenite. The precipitation of cementite from austenite lowers its carbon content and this in turn increases the M_S temperature, so that lath martensite can be a transformation product and this can undergo a self-tempering process, during which other fine, rod-like cementite particles can precipitate. When the carbon content in residual austenite is high enough, it may transform to plate martensite at lower temperatures (below ~473 K). From this it follows that there is not one tempeature at which M-A transforms but a certain temperature interval, e.g. 823-473 K in which some compound of M-A may precipitate. Probably that is the reason why the measurements of M-A transformation temperature were not successful yet.

Residual austenite in M-A constituent was detected as small island close to its martenstic part. Austenite has lower dislocation density than surrounding ferrite. It is suggested that residual austenite may present also as a thin films between the laths of martensite. The crystallographic orientation relationship between the martensite and residual austenite fulfils the Kurdjumov-Sachs orientation relationships. We could not measure the step of tetragonality of martensite as the crystallographic analysis was done by electron diffraction only.

Two shapes of M-A constituent were observed in our study: elongated and massive. From the relatively higher portion of structurally free cementite in elongated M-A, we can conclude that this morphology transformed first (at higher temperatures). But on the other hand we have

observed not only lath but also plate martensite in elongated M-A. Usually lath and plate martensite are mixed together.

As mentioned, we have observed the morphology and distribution of M-A both on polished and etched metallographic surface and on etched fracture surfaces. We have already concluded that when etching the dimpled fracture we could not reveal new M-A particles except for those which were found inside the dimples. But when we etched the cleavage fracture surface, a large amount of M-A could be revealed and this made it possible to make additional conclusions. The distribution and density of M-A in metallographic specimens and fracture surfaces were nearly the same. As mentioned, in well developed crystallographic fracture planes ($\{100\}_{\alpha\text{-Fe}}$) the particles showed some preferred orientation which is seen in Figs. 38a and 38c. Particles were oriented in $\langle 100 \rangle_{\alpha\text{-Fe}}$. While the fraction of elongated and massive particles in metallographic specimen was the same, in fracture surfaces rod-like (elongated) particles prevailed. Explanation of this is the partial disolution of martensite and residual austenite in 'M-A' during etching and the particles visible on the fracture surfaces are then mostly cementite. The preferential growth of cementite in $\langle 100 \rangle_{\alpha\text{-Fe}}$ was found also by Pitch and Schrader[14] as reported in chapter 2.

It is generally accepted that the M-A particle impairs ductility and impact properties of weld. Some papers[16] indicate that during straining the boundary between M-A and matrix is debonded. The boundary between M-A and matrix is but composed of boundaries between cementite and matrix, between residual austenite and matrix and between martensite and matrix. Except for the cementite-matrix boundary, others exhibit high step of coherency so that debonding, like in inclusion-matrix interfaces, is not likely to occur. It is more appropriate to treat the problem as the second phase particles in coarse grained ferritic matrix. No doubt that M-A is detrimental to ductility or upper shelf impact energy. It is a matter for discussion to what extent can M-A itself contribute to increasing the transition temperature. We have shown that M-A can reinitiate the cleavage fracture, but at the same time M-A can hinder the cleavage fracture propagation. Some papers (e.g. 8)) stress the important effect of residual austenite on the embrittlement. As in our case the amount of residual austenite in M-A was low (~2%), we cannot make any conclusion to this point.

We have investigated the decomposition of M-A by tempering or during welding when next welding passes are deposited. We have found that the decomposition of M-A starts at temperatures above 523 K by fine cementite carbides precipitating inside the former M-A and coarser carbide network at the boundary between M-A and matrix. Because fine carbides served the high strength and hardness of former M-A, this stage is not improving toughness yet. Only after re-solution of fine carbides and precipitation of coarser cementite carbides which are more spread in surrounding matrix, the restoration of toughness is expected to occur.

10. Conclusions

1. We have studied the metallography of M-A constituent in HT 80 and HT 100 high strength steel heat affected zone. The M-A (Martensite-Austenite) may consist of retained austenite and martensite and two types of cementite: cementite precipitated at higher temperatures from austenite and cementite produced during lath martensite self-tempering. While cementite precipitating from austenite is coarser, cementite precipitating during the self-tempering of martensite is fine, rod-like or dendrite-like. Two types of martensite were detected in M-A constituent: lath martensite exhibiting high dislocation density and plate martensite in which martensite laths are internally twinned. Retained austenite was detected as small islands inside M-A, exhibiting lower dislocation density than surrounding ferrite matrix. Two morphologies of M-A – elongated and massive – have similar microstructural composition. The orientation relationships between martensite and residual austenite fall into Kurdjumov-Sachs orientation relationships. It is nearly impossible to define certain transformation temperature for M-A constituent. The structurally free cementite can precipitate from austenite at highest temperature (e.g. 773 K). Austenite, depleted by carbon, can partially transform to lath martensite at high M_S temperatures (e.g. 673 K). From this martensite cementite can precipitate in its self-tempering (e.g. 573-473 K). And finally a part of the carbon-rich austenite can transform to plate martensite which has considerably lower M_S temperature (e.g. 473 K).
2. The decomposition of M-A starts at temperatures above 473 K by fine carbide precipitation. Complete decomposition of M-A to ferrite-carbide mixture was, however, observed only above 673 K.
3. The M-A constituent, as second phase particles, is affecting the ductility and impact properties of weld. In the ductile fracture temperature range M-A constituent exhibits appropriate straining ability. At higher strains, however, it fractures or even is fragmented, initiating the dimple fracture formation. Microvoids can initiate also at the interface between M-A and matrix, as a consequence of stress concentration in the matrix. By promoting the initiation of dimples M-A has adverse effect on ductility and upper shelf energy at impact test. In the brittle

fracture temperature range M-A constituent can contribute to cleavage fracture reinitiation. On the other hand, M-A can kink-out or arrest the propagating cleavage crack and increase the fracture energy.

References

1) L.J. Habraken and M. Economopoulos: Symp. Transformation and Hardenability in Steels, Climax Mo. Co., An Arbor, (1967)p.69.
2) I. Hrivnak: Theory of Mild and Microalloyed Steels Weldability, Alfa, Bratislava, (1969).
3) I. Hrivnak: Steels for Electroslag Welding, Metal Constr. & BWJ, (1969)2-s.
4) J. Garland and P. Kirkwood: Towards Improved Sub-merged Arc Weld Metal, Metal Constr., (1976)May/June.
5) F. Matsuda et al.,: Investigation on the Behaviour of M-A Constituent in Simulated HAZ of HSLA Steels, Doc. IIW-IX-1591-90.
6) F. Matsuda et al.: Trans. JWRI, **20**(1991)69.
7) Sub-Commission IX A - IIW (chairman J. Defourny): Guide to Weldability and Metallurgy of Welding of Steels Processed by Thermomechanical Rolling or by Accelerated Cooling, Doc. IIW-IX-1649-91.
8) P. Verrier et al.: Effect of the HAZ Microstructure on the Fracture Toughness of Offshore Microalloyed Structural Steels, Doc. IIW-IX-1645-91.
9) G.R. Speich and W.C. Leslie: Metall. Trans., **3**(1972)1043.
10) T. Terasaki et al.: Proc. Int. Conf. JOM-2, Helsingor, (1984)p.381.
11) C. Dueren: Formulae for Calculating Maximum Hardness in the HAZ of Welded Joints, Doc. IIW-IX-1437-86.
12) N. Yurioka et al.: Metal Constr., (1987)4-271R.
13) G. Krauss: Hardenability Concept with Applications to Steels, AIME, Warredale, (1978)p.235.
14) W. Pitch and A. Schrader: Arch. Eisenhuettenwes, 29(1958)485.
15) H. Ikawa et al.: Trans. JWS, **11**(1980)3.
16) J.H. Chen et al.: Acta Metall., **32**(1984)1779.
17) B. Josefsson and H.O. Andren: Proc. Int. Conf. Recent Trends in Welding Science and Technology, Gatlinburg, Tennessee, (1989)p.243.
18) M.F. Ashby and K.E. Easterling: Acta Metall., **30**(1969)1982.